Cement and Concrete Research 38 (2008) 1232–1245

Contents lists available at ScienceDirect

Cement and Concrete Research

journal homepage: http://ees.elsevier.com/CEMCON/default.asp

Digital laminography assessment of the damage in concrete exposed to freezing temperatures

Kentaro Wakimoto [a], Joshua Blunt [a], Cruz Carlos [a], Paulo J.M. Monteiro [a,*], Claudia P. Ostertag [a], Richard Albert [b]

[a] Department of Civil and Environmental Engineering, University of California, Berkeley, CA 94720, USA
[b] Digiray Corporation, Danville, CA, USA

ARTICLE INFO

Article history:
Received 24 October 2007
Accepted 15 May 2008

Keywords:
Crack detection
Cycles
Laminography
Image analysis
Freezing and thawing

ABSTRACT

The research explores the possibility of using digital laminography as a non-destructive inspection X-ray method to image the damage existing in concrete exposed to low temperatures. Freezing–thawing and scaling tests were performed and digital laminography was used to determine the degree of damage existing inside the concrete samples. First, digital laminography was performed on the concrete sample and then a visual inspection was done by slicing the sample after it was vacuum-impregnated with epoxy in order to compare the differences in crack width.

1. Introduction

The successful evaluation of the extent and severity of cracks caused by frost action is important for determining the life cycle of concrete structures. Visual inspection of concrete surfaces has been standard practice because it is the simplest method, and up until now it has been difficult to evaluate damage inside the concrete. Any robust evaluation of the long-term performance of a structure is difficult without knowing what is happening inside the material. Therefore, non-destructive methods to evaluate the internal damage of concrete structures have been developed to meet these needs.

Typical non-destructive inspection techniques include stress wave propagation and electrical methods [1]. While these methods can evaluate the internal damage of a concrete structure non-destructively, their spatial resolution is low, and visualization using three-dimensional reconstruction is difficult. To complement these methods, X-ray imaging, such as computed tomography and laminography, are being studied [2]. Computed tomography makes it possible to evaluate the internal three-dimensional damage in materials, but the technique has low portability making it hard to transport to the field. The complex geometry and the large dimensions existing in civil engineering structures often prevent the complete distribution of the detectors around the structure, which is required to obtain a sharp image. On the other hand, digital laminography, which is used in dentistry and for inspection of circuit boards, is an attractive methodology to inspect reinforced concrete structures.

This paper reports on the use of digital laminography as a means to determine the presence of cracks and delaminations in concrete exposed to low temperatures. Two specimen types were prepared in order to explore a range of crack types associated with freezing damage. These include internal microcracking and surface scaling [3–5]. Internal cracking from freeze–thaw cycling results in expansion, loss in mechanical properties, and eventually the destruction of concrete [3]. The leading mechanism of destruction is caused by the phase transformation of water into ice, which has a 9% volume expansion. In fully saturated pores of concrete exposed to low temperatures, as volume expansion occurs, the space gets taken up by ice and the unfrozen water is pushed away from the freezing site. The water travels through the porous cement paste until it reaches an air-filled void (escape boundary) where the water freezes avoiding the development of large stress in the matrix [3,6]. If the concrete does not have an adequate air void system, ice is formed in the matrix generating cracks.

Surface scaling, however, is characterized by the loss of small flakes of cement paste or mortar and is limited to a few millimeters near the concrete surface [3,4]. In cold climate conditions, ice forms on the surfaces of bridges and highways. Salt is placed on these surfaces to lower the freezing-point temperature which causes ice to melt, thereby increasing friction on the roadway. A recently proposed mechanism for surface scaling is the bi-material effect. The mechanism of destruction is caused by mismatch in thermal expansion of the

* Corresponding author.
E-mail address: monteiro@ce.berkeley.edu (P.J.M. Monteiro).

0008-8846/$ – see front matter © 2008 Elsevier Ltd. All rights reserved.
doi:10.1016/j.cemconres.2008.05.003

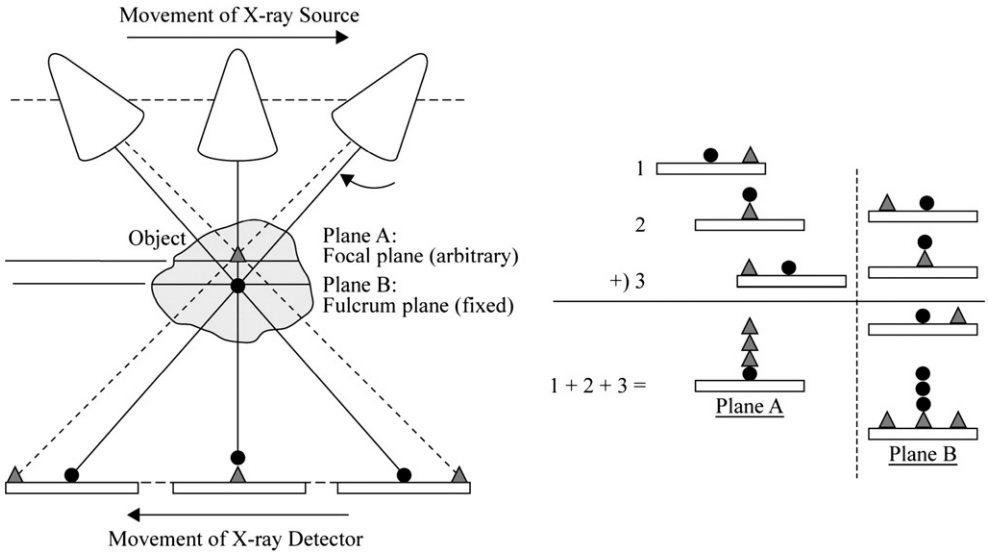

Fig. 1. Illustration of digital laminography (modified from [11,12]).

ice/brine layer and a thin layer at the surface of concrete [7]. Cracking begins in the ice/brine layer and propagates into the concrete surface. Damage is most detrimental at approximately 3% salt concentration and decreases as the concentration increases [5]. At higher salt concentrations, more brine forms and weakens the ice layer, which prevents it from exerting high enough stresses to crack the concrete surface [8].

The following section provides a general overview of digital laminography. Following this, images produced from application of the technique to samples cracked by freeze–thaw and salt scaling are provided. The study concludes with a discussion of the benefits and limitations of the proposed methodology within the scope of the proposed application.

2. Overview of digital laminography

Conventional projection radiography has been widely used since Wilhelm Röntgen invented X-rays in 1895. Although a major breakthrough in clinical diagnostics, it had the inherent limitation of compressing a three-dimensional object into a two-dimensional image. In 1916, the French dermatologist André Bocage proposed using laminography, which could make a specific radiological cross section of the object at a given depth. Together with Massiot, he also developed a laminography device [9,10]. The origin of the word "laminography" is from the "lamino" meaning "thin plate" (laminar) and the Greek word "graphe" meaning "drawing". Laminography is also called geometrical tomography, motion tomography, and conventional tomography.

Since its development, laminography has played an important role in X-ray inspection activity as a new method to replace conventional projection radiography. Once computed tomography was developed for practical use, however, the interest in laminography decreased [11]. Given the limitations in using computer tomography to evaluate large concrete structures, there has been a renewed interest in applying laminography to such structures [2].

Laminography generates a specific radiological cross section by enhancing the contrast of an X-ray image and eliminating structures outside of it by using various projections. These projections are generated by a synchronized motion between an X-ray source and a detector. The acquisition techniques of the projections can be broadly classified into the three types of the synchronized motion between the X-ray source and the detector parallel motion, complete isocentric, and partial isocentric motion. This geometric focusing technique is why laminography is often referred to as geometrical tomography [11,12].

Table 1
Concrete mix proportions for freeze–thaw (FT) and salt scaling (SS) specimens

Material	Weight (kg/m^3)	
	FT	SS
Portland cement	377	400
Water	216	228
Coarse aggregate	812	705
Fine aggregate	901	931

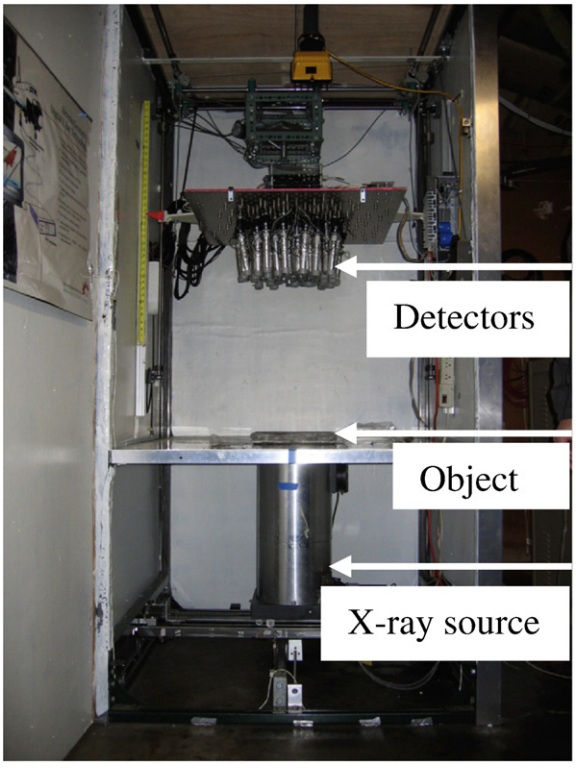

Fig. 2. Motionless Laminography X-ray (MLX®).

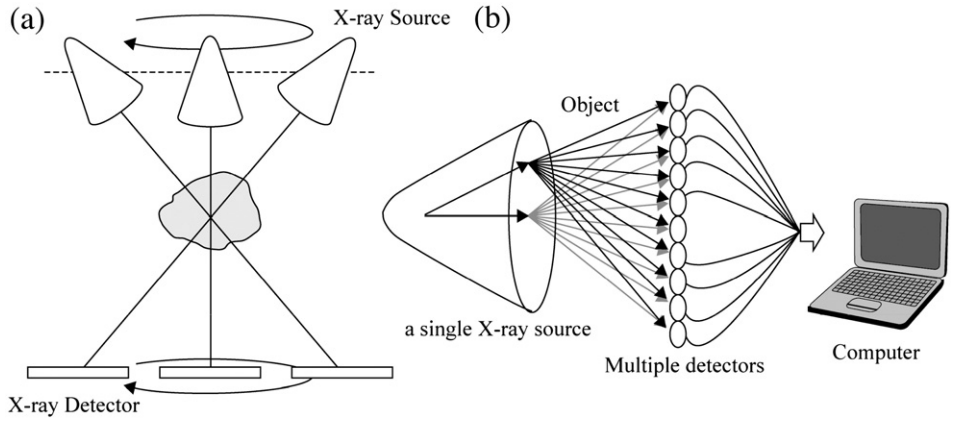

Fig. 3. (a) General digital laminography, (b) Motionless Laminography X-ray (MLX). Illustration of acquisition techniques of projections for general digital laminography and Motionless Laminography X-ray (MLX).

Soon after the invention of laminography in 1916, digital laminography was developed. In 1932, Ziedses des Plantes was the first to demonstrate the concept theoretically whereby it was possible to obtain an infinite number of radiographic cross sections from a series of X-ray exposures. Digital laminography is also called digital tomosynthesis or computed laminography. The origin of the word "tomosynthesis" is from the Greek word "tomo" meaning "slice" and "synthesis" meaning "combining of separate elements". In 1969, Garrison built a prototype three-dimensional roentgenography device that substantiated Ziedses des Plantes's theory [11]. Digital laminography is capable of generating a three-dimensional image, with the added advantage that it is portable.

In digital laminography, various projections are generated by a synchronized motion between an X-ray source and a detector. Fig. 1 demonstrates how digital laminography can be applied where a focal plane for a specific radiological cross section is the same as the fulcrum plane (Plane B). Structures in a focal plane for a specific radiological cross section are always projected to the same position of a detector. Therefore, it is not required to shift the projections during the mechanical integration of them. In digital laminography an arbitrary cross section is considered for a fulcrum plane: that is, a focal plane is not always the same as the fulcrum plane. The object of the focal plane is projected to other positions of the detector; therefore, it is necessary to shift the projections by a length that is dependent on the height of the focal plane during mechanical integration.

3. Experimental program

In the following sections, details regarding specimen preparation for evaluation by digital laminography are provided. Separate specimen types (material and geometry) were used to explore cracking from cyclic freeze–thaw (FT) damage and surface salt scaling (SS). Visual evaluation of the cracking was carried out in two parts; (1) through the use of a proprietary digital laminography system and (2) from direct visual evaluation of a cut surface.

3.1. Specimen preparation

Mix proportions for both the FT and the SS are provided in Table 1. The cement was an ASTM C150 Type II and the fine aggregate consisted of a coarse river sand (bulk specific gravity = 2.65, fineness modulus = 3.2). The coarse aggregate for the freeze–thaw specimens was a 10 mm maximum sized pea gravel (bulk specific gravity = 2.76) while the coarse aggregate for the salt scaling specimens was a 6 mm maximum sized crushed gravel (bulk specific gravity = 2.68). Different aggregate sizes were chosen based on the minimum specimen dimensions (discussed below) which, in order to use a cohesive concrete mix, resulted in the observed variances between the mix designs.

The freeze–thaw specimen was a prismatic element with dimensions of 76 × 76 × 286 mm. The scaling specimens were relatively flat, plate-like elements 305 × 305 × 25 mm in size. The difference in specimen geometry reflects the nature of the proposed damage techniques. Freeze–thaw cracking is an internalized phenomenon, so depth and width were increased in order to provide a larger cross section through which cracks could develop and propagate. Scaling is typically located at the element surface, so specimens were relatively thin with a broad surface in order to maximize the area available to damage.

All mixing was carried out in a 20 L planetary mixer and specimens were covered and stored in their molds for 24 h after which the molds were removed and the specimens were placed in a fog room (100% relative humidity, 23 °C) until testing. Freeze–thaw cracking was induced in accordance with ASTM C666 and approximately 1 week of cycling was necessary in order to produce a network of visible surface cracks. Scaling

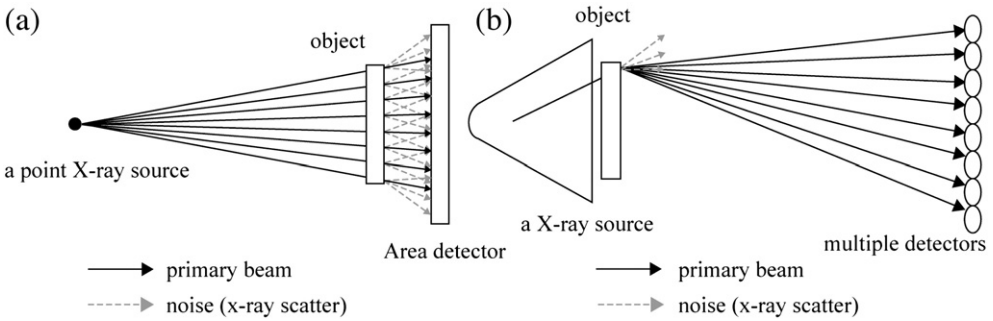

Fig. 4. (a) General digital laminography, (b) Reverse Geometry X-ray ® (RGX®). Illustration of geometry of an X-ray source and detector(s) for general digital laminography and Reverse Geometry X-ray (RGX).

Table 2
Scanning setup for all specimens

	Scanned area (mm)			Image matrix (pixel)		# of slices	Spatial resolution	
	Width	Height	Depth	Width	Height		*x*–*y* (mm/pixel)	*Z* (mm/slice)
FT[a]	107.0	115.0	78.0	608	656	300	0.176	0.260
SS 1	63.5	67.0	38.1	944	1000	150	0.067	0.254
SS 2	63.5	65.0	38.1	968	1000	150	0.065	0.254

[a]Steel wire was placed on the specimen surface as a reference scale.

was carried out per ASTM C672 and different degrees of cracking were induced by putting the sample through 3 and 11 scaling cycles.

3.2. Digital laminography

The digital laminography equipment used in this research was the Motionless Laminography X-ray (MLX®) developed by Digiray® Corp. This device is shown in Fig. 2. MLX has two advantages over general digital laminography (see Fig. 3). First, it is motionless. The motionless system of MLX is accomplished by combination of a single X-ray source, multiple detectors, and software that compares data from each detector. While computed tomography, micro computed tomography, and general digital laminography rely on relative movement between the X-ray source and the detector, MLX employs no moving parts. Second, MLX is based on Reverse Geometry X-ray (RGX®) radiography. The difference between general digital laminography and RGX is schematically illustrated in Fig. 4. RGX is accomplished by combination of reverse geometry of device and multiple detectors. While a conventional system places an object close to a large-area detector, RGX places the object in close proximity to an X-ray source. Better images are obtained because small, distant detectors preferentially capture primary X-rays without scattered radiation [13]. The two-dimensional spatial resolution is dependent on the magnitude of zoom and can be as low as 12 μm. A spatial resolution in the third dimension of 200 μm has been obtained. The MLX system is also portable.

Digital laminography using MLX was performed for all specimens. A 100.08 kV power source was used and the detector array was placed 686 mm from the X-ray emitter. Specimens were exposed to the X-rays for 240 s. Other pertinent information regarding the scanning setup is provided in Table 2. For the second freeze–thaw image scan a steel wire (0.75ϕ×30 mm) was attached to the exterior surface of the specimen in order provide a reference scale.

3.3. Visual inspection and vacuum epoxy impregnation

Optical scans were performed on the surfaces of interest for all samples in order to compare with results obtained by digital laminography. Crack width and length were measured using a crack comparator. However, in order to observe internal cracking, the freeze–thaw sample was vacuum-impregnated with epoxy and slices

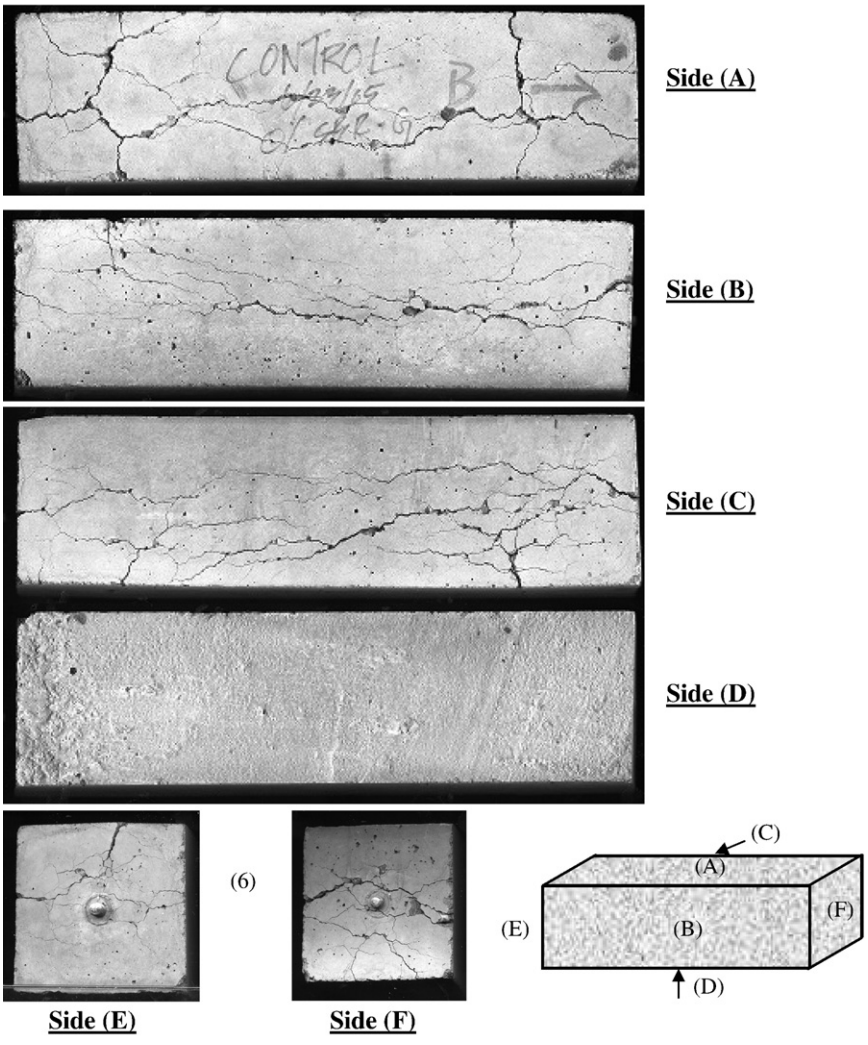

Fig. 5. Optical scan images of FT specimen exterior after freeze–thaw cycling.

were cut in order to observe the internal damage. The procedure of vacuum epoxy impregnation is described below:

(a) Samples were placed in a container and evacuated for 30 min at a constant −101.6 kPa in a vacuum chamber.
(b) The sample holder was filled with epoxy resin stained with blue dye that was introduced into the chamber while maintaining the vacuum.
(c) Samples were submerged into the epoxy resin and were kept under vacuum for an additional 30 min.
(d) Finally, the samples were removed from the vacuum chamber and cured in a closed oven for 5 h at a temperature of 50 °C until the epoxy resin hardened.

4. Experimental results and discussion

4.1. Freeze–thaw (FT) specimen

Optical image scans of the specimen exterior after the freeze–thaw cycling are shown in Fig. 5. The images acquired with MLX are shown in Fig. 6. The image numbering convention is such that image #1 corresponds to side C (see Fig. 5) and the final image (#300) corresponds to side B. Each successive image from #1 to #300 represents an internal section as one moves through the specimen from side C to side B.

An optical scan image and a digital laminography image of an internal section for the FT test sample are shown in Fig. 7. The optical scan was performed on a section that was cut from the middle of the

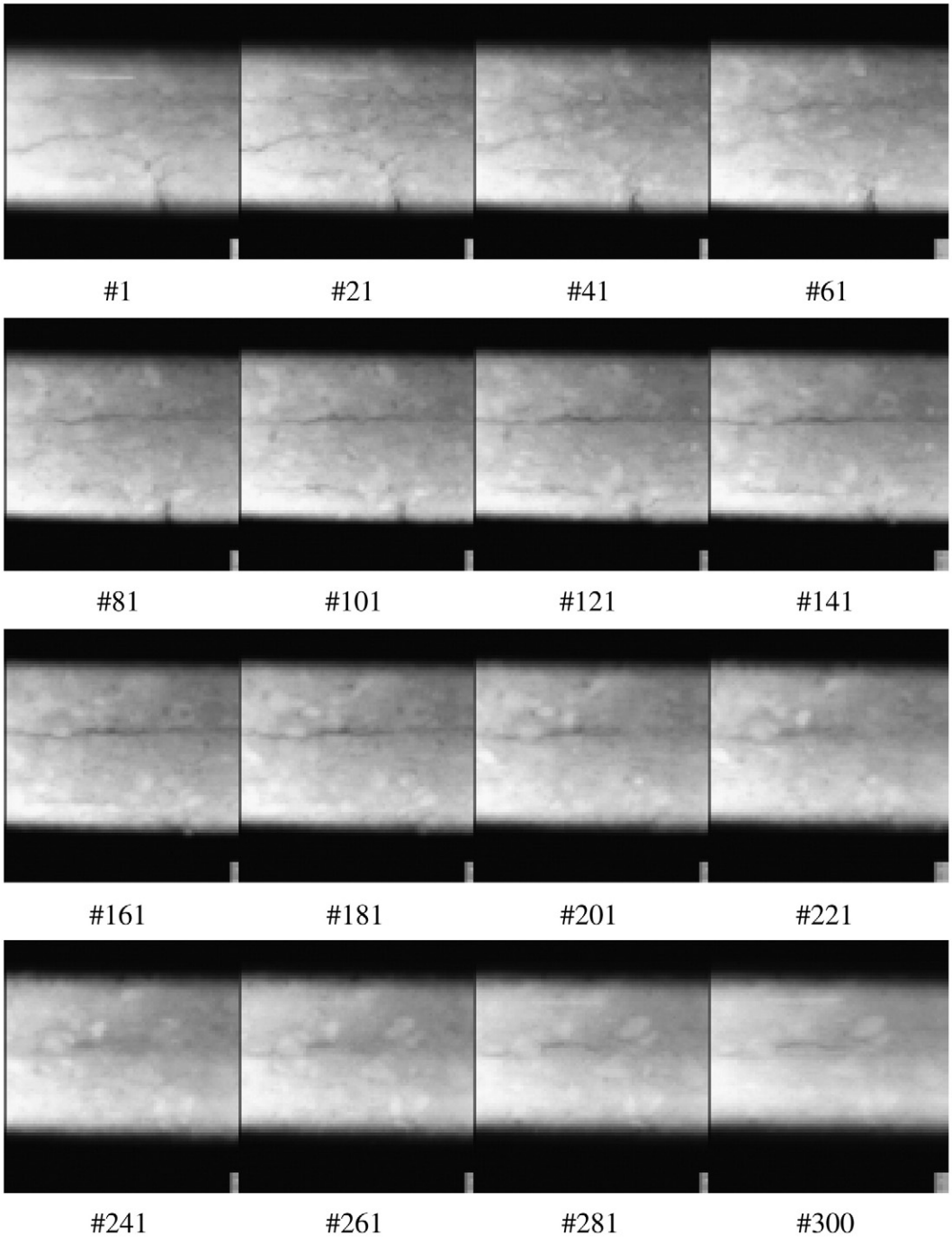

Fig. 6. MLX through-thickness images of the FT specimen (image #1 is side C and image #300 is side B).

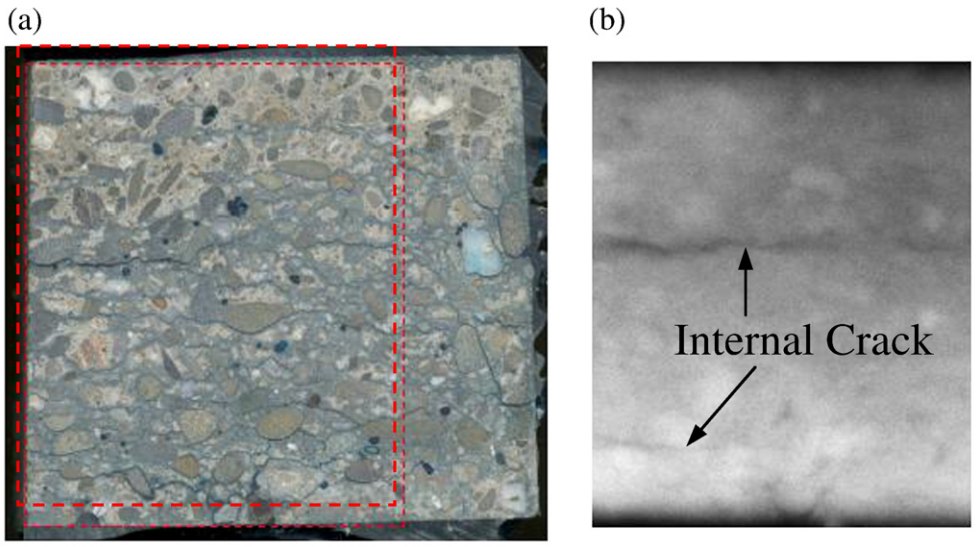

Fig. 7. Comparison of internal cracks observed in an optical scan image and digital laminography scanned image from the FT specimen (a) optical scan of an internal section, (b) digital laminography scanned image (image #100).

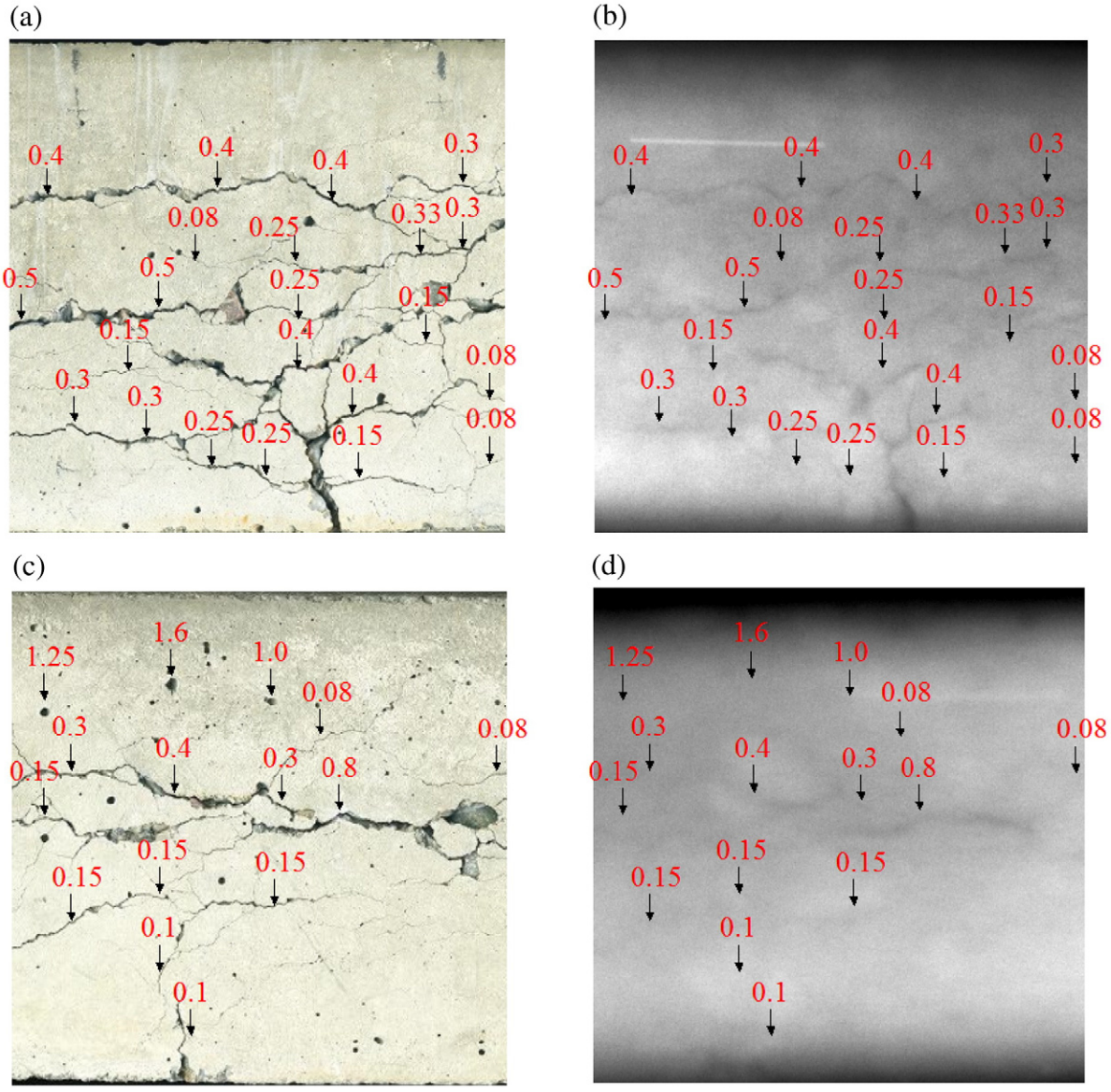

Fig. 8. Comparison of detectable crack width using optical and digital laminography images of FT sample; (a) optical scan image on side C, (b) digital laminography scanned image #1 (c) optical scan image on side B, (d) digital laminography scanned image #300.

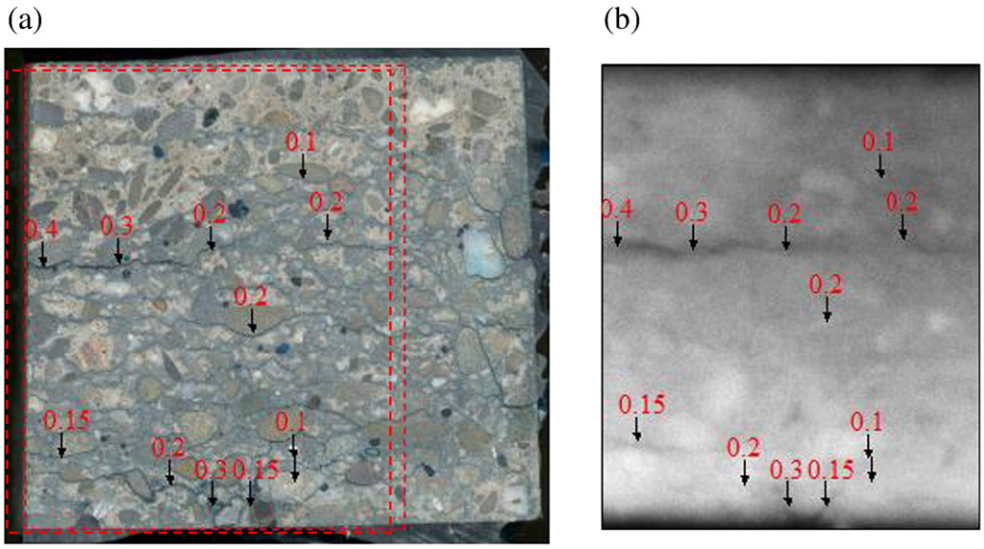

Fig. 9. Comparison of detectable crack width using optical and digital laminography images of an internal section of the FT sample; (a) optical scan image of an internal section, (b) digital laminography scanned image #100.

specimen after vacuum epoxy impregnation. The digital laminography image was #100 from the FT series (represents a depth of 25 mm from side C). Some internal cracks were observed in the digital laminography scanned image, and the location of the cracks is similar in the two images.

The minimum detectable crack width for the FT sample using digital laminography was determined by comparing the measured values of the specimen (obtained directly with a crack comparator) with a corresponding digital laminography image. These comparisons are provided in Figs. 8–10. Digital laminography detected cracks 0.25 mm or wider on the exterior surface of each sample and from Fig. 8 it is shown that the minimum detectable crack width on side B is less than that of side C. Also, small round voids present in the exterior surface of side B were not visible by digital laminography. If the resolution is increased by narrowing down a test area, cracks less than 0.15 mm wide may be seen.

An optically scanned image and a digital laminography scanned image of a cut section from the freezing and thawing test sample are shown in Fig. 9. Digital laminography detected cracks 0.2 mm or wider.

A magnified view of the digital laminography scanned image from side C of the FT test sample is shown in Fig. 10. Digital laminography was able to image the difference between a 0.3 and a 0.5 mm crack width. It is difficult to evaluate the width of a small crack using the digital laminography scanned images because the boundary between crack and concrete is obscure.

Distortion of digital laminography scans was investigated by comparing optically scanned images and digital laminography scanned images on the surface of the sample. This is shown in Fig. 11. Points along the surface cracks were used as reference. The reference points and the points measured by digital laminography were overlapped. Based on this method and the specimen under investigation, the spatial distortion using digital laminography was less than 10%.

Image #1 and #20 of the FT sample series acquired with digital laminography are shown in Fig. 12. A 0.75 mm diameter wire was attached to the exterior surface (side C) as a reference point and can be observed in both images. The spatial difference between image #1 and #20 is a depth of 5 mm, which is much greater than the diameter of the wire. Because of this it can be said that the presence of the wire in image #20 (Fig. 12(b)) is an artifact of the current MLX reconstruction process.

Although digital laminography uses two-dimensional images projected along the direction of the X-rays, the contrast of the images

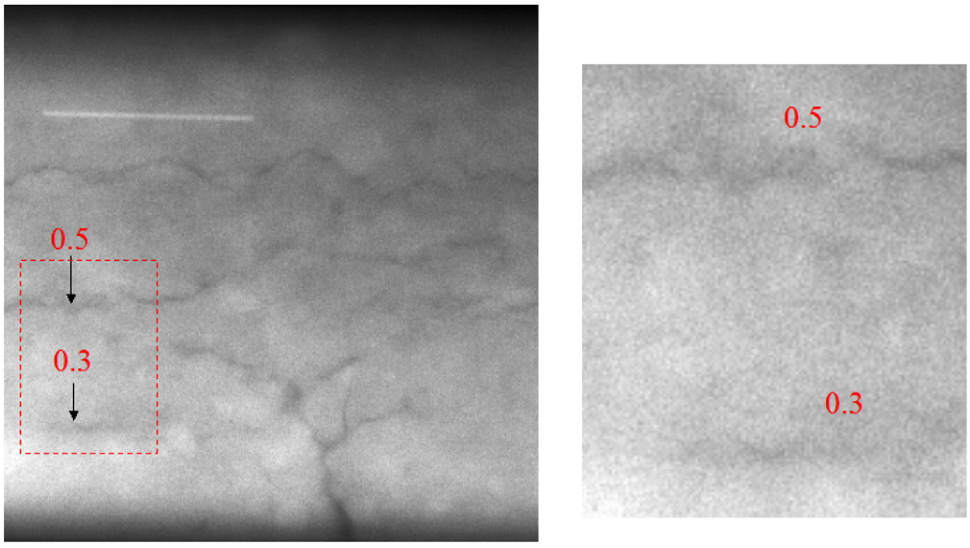

Fig. 10. Magnified view of digital laminography scanned image #1 of FT sample.

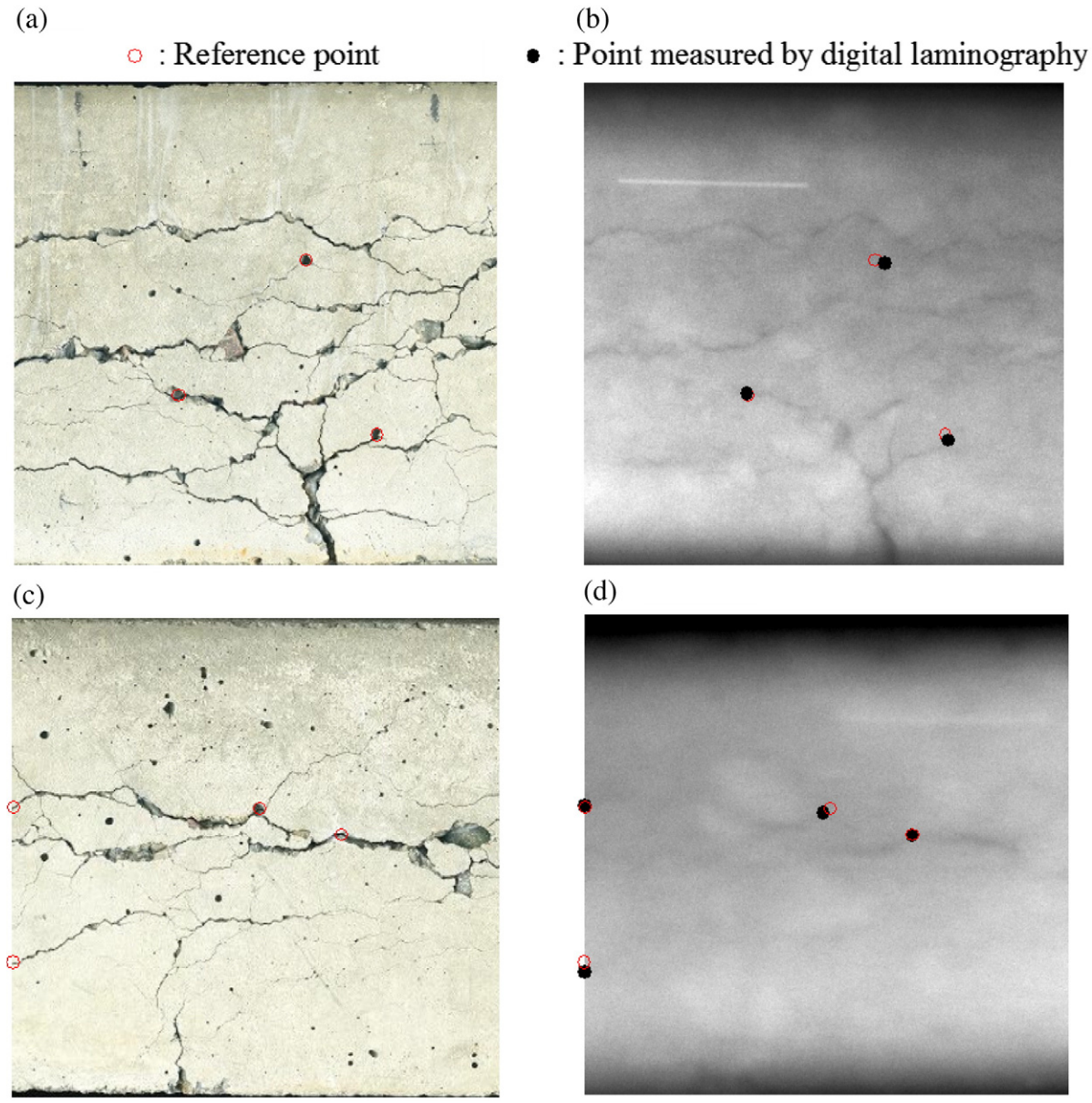

Fig. 11. Comparison of void location in the FT test sample obtained from optically scanned images and digital laminography scanned images; (a) optical scan image on side C, (b) digital laminography scanned image #1, (c) optical scan image on from side B, (d) digital laminography scanned image #300.

is enhanced by mechanical integration. Three-dimensional reconstructed images for the FT test sample using all of the planar digital laminography scanned images are shown in Fig. 13. Reconstruction provides a means to visualize through-thickness cracking so that out of plane conditions can be analyzed.

A comparison between an optical image and a two-dimensional cross section extracted from the through-thickness three-dimensional reconstruction is shown in Fig. 14. Although through-thickness cracking was observed in the optical image, the majority of these cracks were not easily visible in the trough thickness reconstruction. This shows that structures along the direction of the X-ray are not reconstructed as clearly as those which are perpendicular to the direction of the X-ray.

4.2. Salt scaling (SS) specimen

Fig. 15 provides photos of the SS specimen after various stages of salt scaling. Digital laminography images are shown in Figs. 16 and 17. The image numbering convention is similar to the FT specimen in that successive images represent movement through the thickness of the sample, however only 150 slices were reconstructed (as opposed to 300 for the FT specimen). Image #150 represents the top surface as shown in Fig. 15 (the top surface per the convention of this study is the one upon which solution was ponded during cyclic salt scaling). A digital photo and a digital laminography image for the scaling test sample after 3 cycles are shown in Fig. 18. The digital laminography scanned image was the #51 out of 150 slices. The depth of the slice from the top surface was 17 mm. While no cracks were observed on the top surface, internal cracks, coarse aggregates, and air voids were observed in the digital laminography scanned image, indicating that digital laminography located internal cracks in the sample.

Fig. 19 compares the internal cracks existing in a sample after 3 and 11 cycles by digital laminography. The images represent layer #150, which is the top most layer provided by the MLX reconstruction. They are the best representation of behavior at the top surface. Many more cracks are observed on the specimen after 11 cycles than after 3 cycles, therefore digital laminography was capable in monitoring the evolution of damage in the samples.

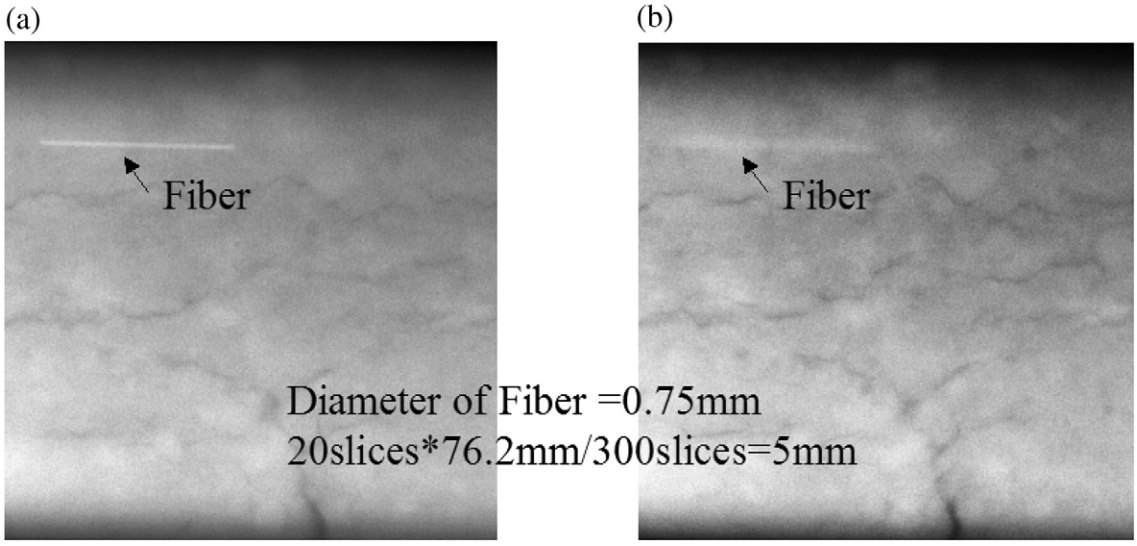

Fig. 12. Artifact of the fiber on FT test sample by digital laminography: (a) image #1 (b) image #20.

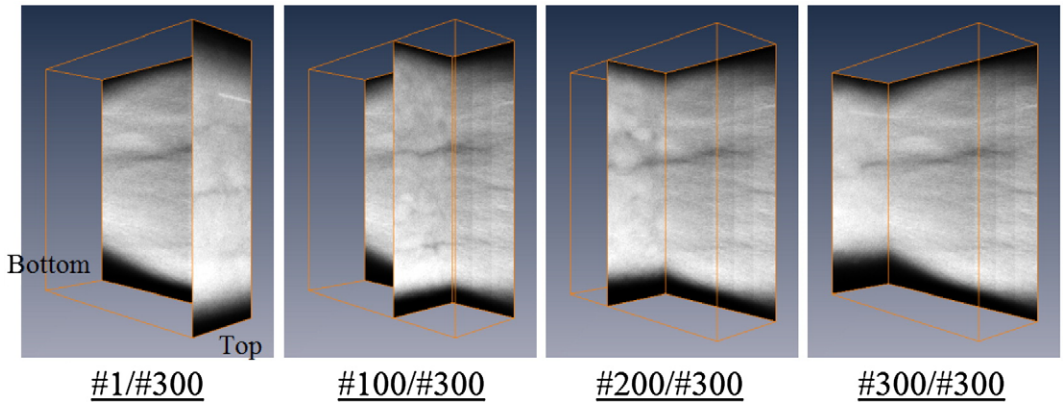

Fig. 13. Three-dimensional reconstruction images of the FT test sample using all the digital laminography scanned images.

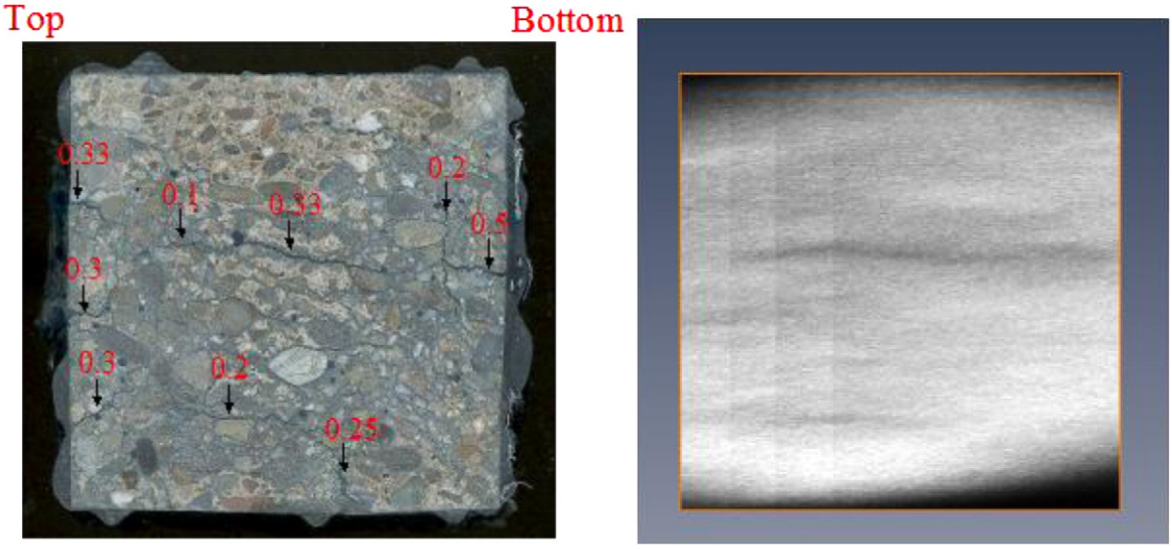

Fig. 14. Comparison of internal cracks of freezing and thawing test sample between photo of sample and two-dimensional cross section extracted from the three-dimensional image.

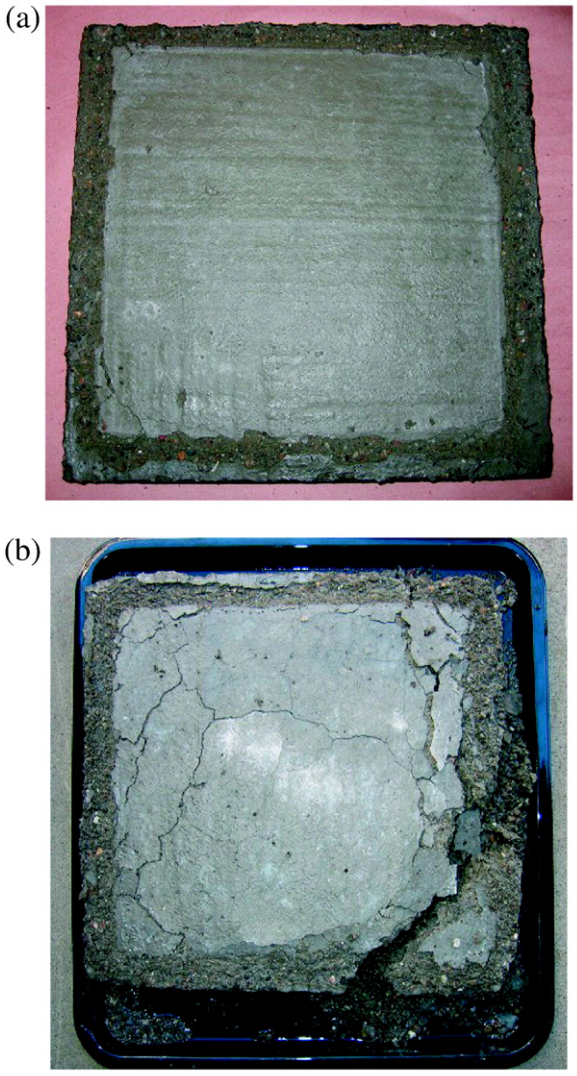

Fig. 15. (a) after 3 cycles (SS 1), (b) after 11 cycles (SS 2). Photos of SS specimen after cyclic salt scaling.

Another artifact is observed between image #51 and image #141 within the SS 2 image series (11 scaling cycles). These images, acquired with digital laminography, are shown in Fig. 20. The void in the center of the sample can be observed in both images. Using the fiber as a scale reference, the diameter of the void measured in the plane of the image is about 4 mm. However, the apparent depth of void penetration is about 23 mm because the space of each image layer is 0.25 mm. Similar to the behavior of the fiber in the FT image series, this represents a rather large through-thickness artifact because a more reasonable assumption is that the void is spherical in shape and should only be visible through a depth of 4 mm.

5. Extended discussion on digital laminography

Throughout this investigation it was noted that the cross sections reconstructed by digital laminography were still artifact-inherent (Figs. 12 and 20). This through-thickness blur is attributed to the simplistic nature of the reconstruction process which employs a "shift-and-add" technique to produce the backprojections. It is a software limitation in the current setup and should not be attributed in anyway to hardware. Algorithms have been studied that could eliminate the artifacts. For example, the application of filtered backprojection used for computed tomography [14] has been applied for use in digital laminography. Other tools, such as line tracing algorithms [15], which can be applied directly to the backprojections as a post-processing technique, may have application for crack tracing that can reduce the blur in the individual backprojections. Only with improved image quality should through-thickness 3-d reconstructions be attempted, because the blur introduced by the current reconstruction method compounds when the backprojections are integrated.

An interesting phenomenon was also observed in the FT specimen MLX image series (Fig. 6). Image #1 appeared less blurred and of higher quality than image #300. This was highlighted in Fig. 8, where the cracking on the exterior surfaces of the specimen was of similar nature, yet the MLX backprojections showed less cracking on one side when compared to the other. Behavior such as this accents the importance of the geometrical nature of the setup. The quality of the image depends on the shape of the sample, and how it is oriented relative to the X-ray tube and detector array. Image #1 (Fig. 6) represents the surface of the FT sample that was placed directly against the X-ray tube. As one moves through the thickness of the sample and gets further away from the tube a phenomenon known as detector drop-off can occur. This occurs in thicker samples because the direction of the X-rays that penetrate the sample surface furthest from the X-ray source is such that they are not seen by the peripheral detectors. When fewer projections are available for the reconstruction process, backprojection image quality is reduced. Of course this can be remedied by moving the detectors further from the X-ray source; however constraints such as a ceiling in the current setup (see Fig. 2) may be the limiting factor.

The previous discussion points out the need to determine an optimal specimen geometry for quality imaging with the proposed MLX setup. In addition to the geometric constraints of detector drop-off, it is noted that the imaging technique utilizes attenuated X-ray intensity as it propagates through an object. Image contrast is therefore a function of the X-ray power source and the composition of the different phases inside the concrete matrix. Specimen thickness also plays a role; if a specimen is too thick then all the X-rays can be absorbed and the projections will appear washed out. Thinner elements such as slab and wall structures would be ideal. An elevated reinforced concrete deck slab would allow one to access both surfaces for easy application of the MLX technique. It is proposed that MLX may also have application in large column and beam elements as a means to visually examine the nature of the cover concrete. However creative ways to position the detector array need to be developed and tested.

6. Conclusions

From the work done in this research, the following conclusions can be made:

The test results indicate that digital laminography is able to locate internal cracks in concrete samples and monitor the evolution of damage in the concrete.

Digital laminography detects cracks 0.25 mm or wider on the surfaces of concrete samples placed against the X-ray tube; however the minimum detectable crack width increases as one moves through the sample, further from the X-ray source.

Digital laminography is able to evaluate the difference in crack width; however, it is difficult to evaluate the width of small cracks using the digital laminography scanned images because the boundary between crack and concrete is obscure.

The distortion of a digital laminography scanned image is less than 10%.

Digital laminography is able to evaluate the three-dimensional geometry of cracks; however, the depth of cracks is not accurate because of the artifacts inherent in digital laminography. In its current

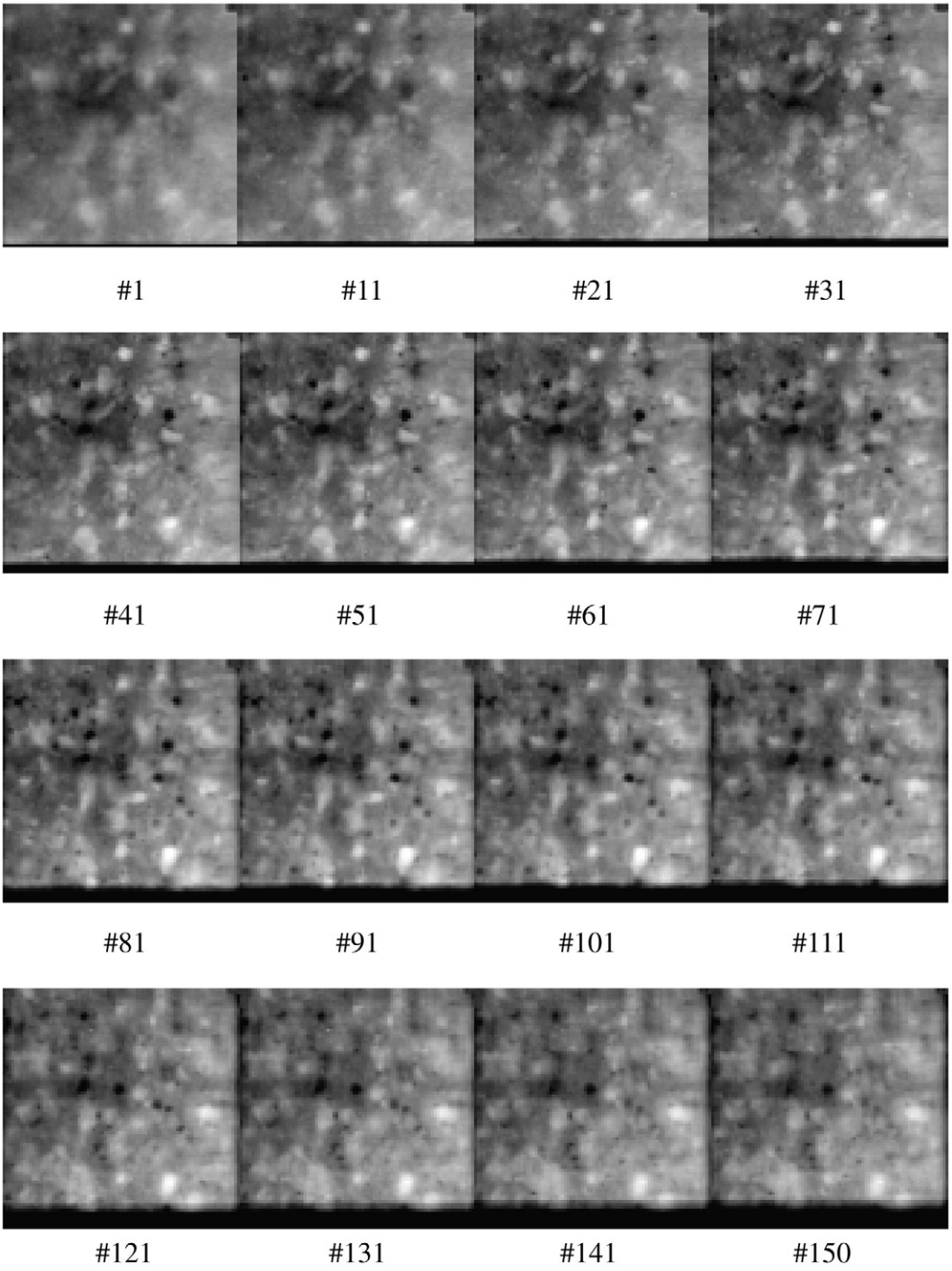

Fig. 16. SS 1 series MLX through-thickness images.

state, the structures perpendicular to the X-ray can be recorded more clearly than those parallel to the direction of the X-ray.

Acknowledgment

Paulo Monteiro wishes to thank the support given by KAUST.

References

[1] P.K. Mehta, P.J.M. Monteiro, Concrete: Microstructure, Properties and Materials, third editionMcGraw Hill, 2006.
[2] V. Fariborz, C.P. Ostertag, P.J.M. Monteiro, R.D. Albert, Damage characterization of concrete panels due to impact loading by motionless X-ray laminography, Journal of Materials Science 42 (9) (2007) 3280–3285.
[3] M. Pigeon, R. Pleau, Durability of concrete in cold climates, in: A. Bentur, S. Mindess (Eds.), Modern Concrete Technology Series, E & FN Spon, London, UK, 1995.
[4] J. Marchand, R. Pleau, R. Gagne, Deterioration of concrete due to freezing and thawing, in: J. Skalny, S. Mindess (Eds.), Materials Science of Concrete IV, American Ceramic Society, Westerville, OH, 1995.
[5] G.W. Scherer, J.J. Valenza, Mechanisms of frost damage, in: F. Young, J. Skalny (Eds.), Materials Science of Concrete VII, American Ceramic Society, Westerville, OH, 2005.
[6] T.C. Powers, Freezing effects in concrete, Durability of Concrete, American Concrete Institute, Detroit, MI, 1975.
[7] J.J. Valenza, G.W. Scherer, A review of salt scaling: II. Mechanisms, Cement and Concrete Research 37 (7) (2007) 1022.
[8] O. Copuroglu, E. Schlangen, Modeling of frost salt scaling, Cement and Concrete Research 38 (1) (2008) 27–39.
[9] R. Van Tiggelen, In search for the third dimension: from radiostereoscopy to three-dimensional imaging, JBR-BTR 85 (2002) 266–270.
[10] R. Van Tiggelen, Since 1895, orthopaedic surgery needs X-ray imaging: a historical overview from discovery to computed tomography, JBR-BTR 84 (2001) 204–213.

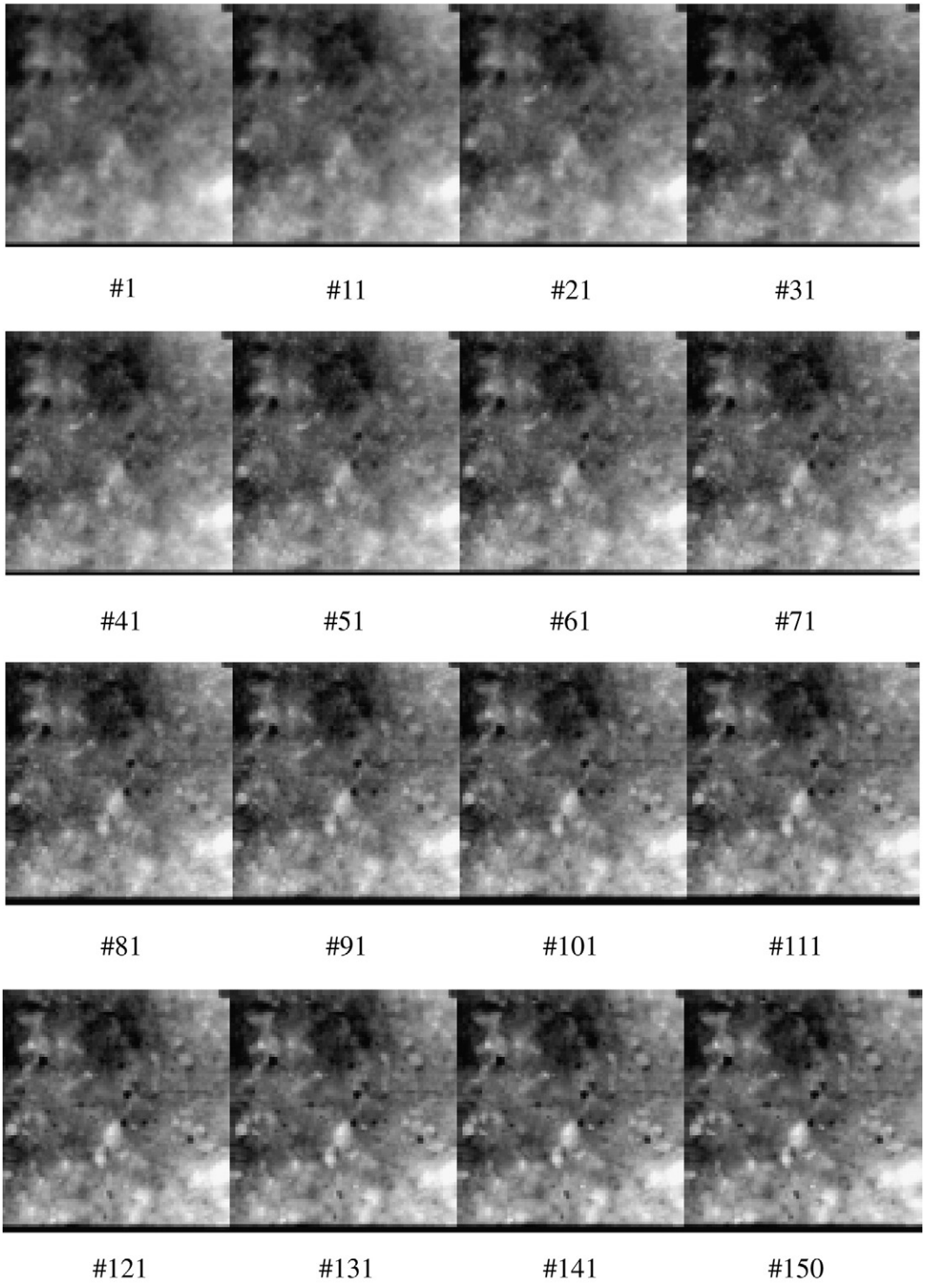

Fig. 17. SS 2 series MLX through-thickness images.

[11] J.T. Dobbins, D.J. Godfrey, Digital X-ray tomosynthesis: current state of the art, Phys. Med. Biol. 48 (2003) R65–R106.
[12] C. Bernhardsson, Digital Tomosynthesis: Fundamental Principles and Comparison to Conventional X-ray Imaging, Master of Science Thesis, Medical Radiation Physics Clinical Sciences, Lund University, 2006.
[13] Digiray Corporation, Technology Overview of Digiray Reverse Geometry X-ray Imaging, Internet Resource, Oct. (2007), <http://www.digiray.com/technology.htm>.
[14] G. Lauritsch, W.H. Haerer, A theoretical framework for filtered backprojection in tomosynthesis, Proceedings of the SPIE Conference on Image Processing, San Diego, California, 1998, pp. 1127–1137.
[15] E. Meijering, M. Jacob, J. Sarria, P. Steiner, H. Hirling, M. Unser, Design and validation of a tool for neurite tracing and analysis in fluorescence microscopy images, Cytometry Part A 58A (2004) 167–176.

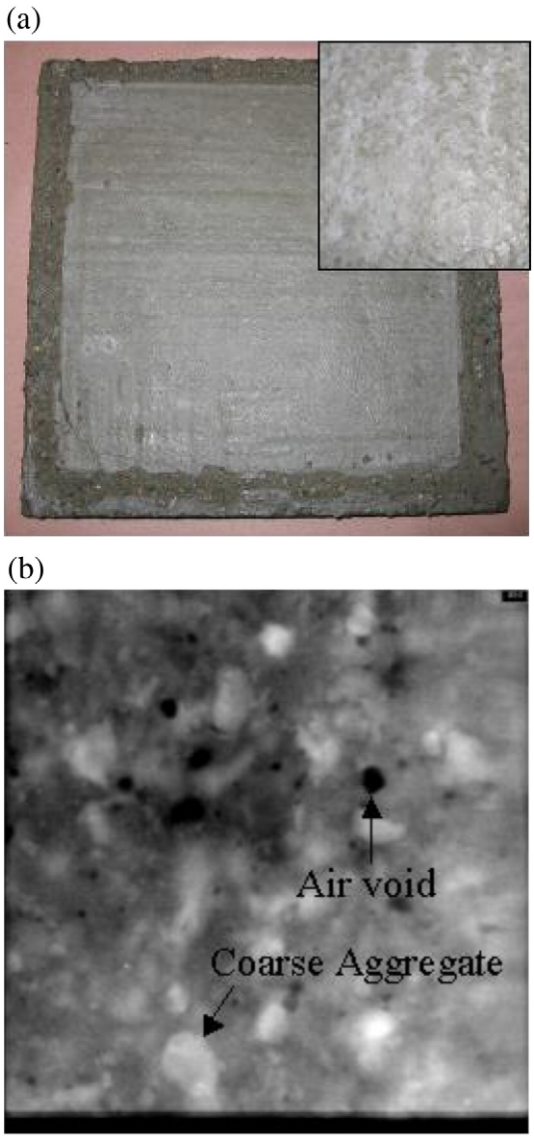

Fig. 18. Comparison between surface cracks visible in a digital photo and internal cracks visible in digital laminography scanned image for a scaling test sample after 3 cycles (SS 1); (a) photograph, (b) digital laminography scanned image #51.

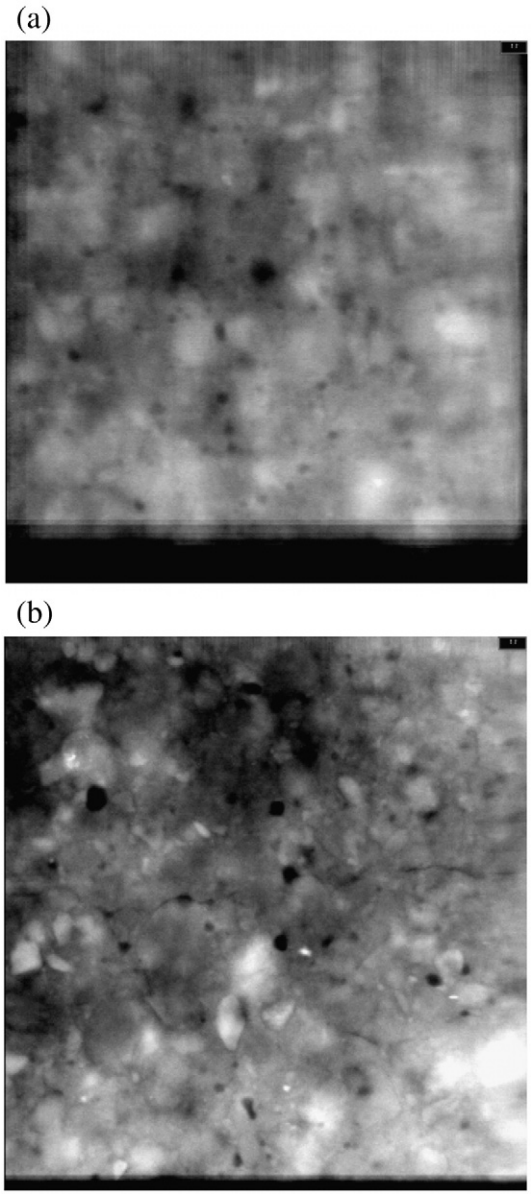

Fig. 19. Comparison of surface cracks of scaling test sample between after 3 cycles and 11 cycles by digital laminography; (a) Image #150 after 3 cycles (SS 1), (b) Image #150 after 11 cycles (SS 2).

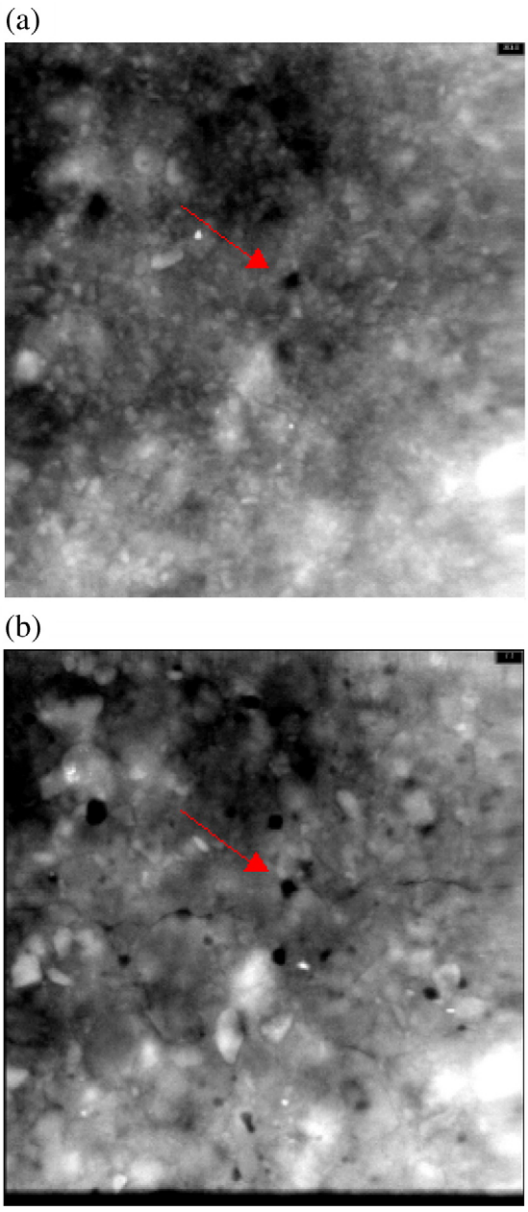

Fig. 20. Artifact of void of scaling test sample SS 2 by digital laminography: (a) image #51, (b) image #141.